Vrije Universiteit Brussel

Faculteit Wetenschappen en
Bio-ingenieurswetenschappen

Departement Natuurkunde

Search for Dark Matter in the Monojet and Trackless Jets Final States with the CMS Detector at the LHC

Isabelle De Bruyn

Promotor

Prof. Dr. Steven Lowette

Acknowledgements

Table of Contents

1
Introduction

2

Dark Matter Scenarios Beyond the Standard Model

2.1 The Standard Model of Particle Physics

2.1.1 Elementary particles and their interactions

2.1.2 Unanswered questions of the Standard Model

2.2 Dark matter

2.2.1 Observational evidence

2.2.2 Detection of dark matter

2.2.3 Dark matter models

2.3 Strongly Interacting Massive Particles

2.3.1 Motivation

2.3.2 Experimental constraints

3

The LHC and the CMS Detector

In order to investigate the currently unsolved mysteries of particle physics, such as the existence of dark matter, many experiments can be conducted, among other things at particle colliders. The largest particle accelerator in the world is the Large Hadron Collider (LHC), located at the European Organization for Nuclear Research (CERN) in Geneva, Switzerland. At this accelerator, protons are being accelerated at energies up to 6.5 TeV, giving rise to a record center-of-mass energy of 13 TeV in the proton collisions. Using data from the collisions generated at the interaction points along the accelerator ring, the Standard Model can be tested in many ways and searches for particles beyond the Standard Model can be performed.

In Section 3.1 more details are given about the LHC and the 4 main experiments situated at the interaction points. In particular, the general-purpose Compact Muon Solenoid (CMS) detector is described in Section 3.2.

3.1 The Large Hadron Collider at CERN

The LHC was built in the already existing Large Electron Positron (LEP) collider tunnel, which was excavated in the 1980's and has a circumference of 27.6 km. Contrary to the LEP collider, the LHC accelerates particles of the same charge, namely protons or lead ions. Much higher luminosities can therefore be reached, since only particles are used and the generation of anti-particles is not needed. Additionally, the colliding particles are not the protons or ions, but the constituents of the hadrons, which cover a wide energy range. This makes the LHC the ideal instrument to explore unknown territory.

3.1.1 The LHC injector chain

The protons (or lead ions) can not directly be injected in the LHC, but need to be accelerated gradually in several pre-accelerators, as illustrated in Figure 3.1. For the proton beams, the LHC injection chain starts at a bottle of hydrogen, where protons are stripped from the hydrogen atoms and accelerated up to 50 MeV by a linear accelerator (LINAC2). The protons are then transfered to a chain of circular accelerators, starting with the Proton Synchrotron Booster (PSB) which accelerates them to an energy of 1.4 GeV. Next, the protons go through the Proton Synchrotron (PS) and are delivered to the Super Proton Synchrotron (SPS) at an energy of 26 GeV. Finally, the protons are injected in the LHC in opposite direction with an energy of 450 GeV. In the LHC the protons are then accelerated to 3.5 TeV (in 2010 and 2011) or 4 TeV (in 2012) during Run 1, and to 6.5 TeV during Run 2 (since 2015).

The lead ions are first accelerated in a different linear accelerator, LINAC3, before being injected in the Low Energy Ion Ring (LEIR) at an energy of 4.5 MeV per nucleon. Here the ions are accelerated

to an energy of 72 MeV per nucleon, and they then follow the same path as the protons through the PS, where they are accelerated to 5.9 GeV and stripped from the last of their electrons, and the SPS, where they are accelerated to 177 GeV. The record center-of-mass energy for heavy ion collisions at the LHC so far has been 5.02 TeV and 8.16 TeV, for lead-lead (Pb-Pb) and proton-lead (p-Pb) collisions in 2015 and 2016 respectively.
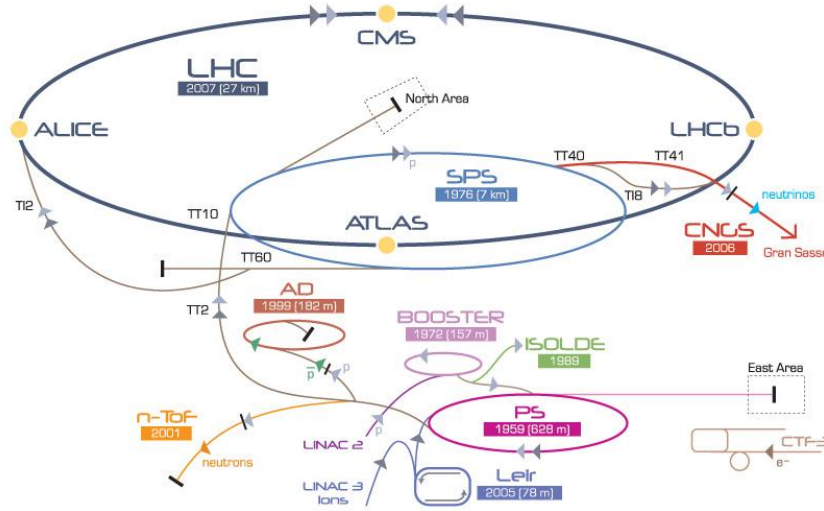

Figure 3.1: Schematic view of the various linear and circular accelerators of the CERN accelerator complex, including the LHC injection chain.

3.1.2 The Large Hadron Collider

The most relevant specifications for a particle physics accelerator are the maximum energy and the luminosity that can be reached. High energy is necessary in order to be able to create new heavy particles, which are for example predicted in many theories beyond the Standard Model. A high event rate or luminosity $\mathcal{L}$ is equally important, to obtain a sufficiently high number of collisions. For a process with cross section σ, this rate is

$$\frac{dN}{dt} = \mathcal{L}\sigma. \tag{3.1}$$

In order to achieve the high design luminosity of 10^{34} cm^{-2}s^{-1}, the protons are focused in bunches with a 25 ns spacing by strong quadrupole magnets around the interaction regions. Additionally, 225 ns gaps are present as well between the bunch batches, corresponding to the rise time of the injection kicker magnets. One gap of 3 μs is necessary as well to allow clean beam dumps. These requirements limit the number of bunches to a maximum of 2808.

Since the collisions happen between bunches of protons, multiple protons will be colliding at the same time. The extra collisions, next to the potentially interesting collision, are referred to as pile-up interactions. The particles generated in these collisions are all detected simultaneously and form a challenge for the physics experiments to disentangle them from the particles coming from the to be studied interaction.

The bunches are kept on the correct orbit by the 1232 LHC dipole magnets. These magnets are cooled down to 1.9 K with liquid Helium and supplied with a current of 12 kA to reach the design field of 8.33 T. This limits the maximum beam momentum of the accelerator to

$$p = B/\rho = 8.33\,\text{T}/2804\,\text{m} = 7\,\text{TeV/c}, \tag{3.2}$$

with ρ the bending radius of the tunnel. The protons are accelerated up to the desired energy by radio-frequency (RF) cavities, which produce an oscillating electromagnetic field. As a consequence, late or early protons will feel an acceleration or deceleration, respectively.

After almost 25 years of design and construction, the LHC was completed in 2008 and the commissioning of the machine started. However, a mechanical incident on 19 September of the same year delayed the first collisions, at a beam energy of 900 GeV, until late 2009. During 2010 and 2011 a center-of-mass energy of 7 TeV was used for the collisions, which was then increased to 8 TeV in 2012. The instantaneous luminosity was also increased, starting from 2×10^{32} cm^{-2}s^{-1} in 2010 to more than 6×10^{33} cm^{-2}s^{-1} in 2012. During the 3 years of data-taking in Run 1, data corresponding to an integrated luminosity of 45.0 pb^{-1}, 6.1 fb^{-1}, and 23.3 fb^{-1} respectively, were delivered. After Run 1, a long shutdown (LS1) of 2 years followed, which was used to correct the problems that were discovered in the aftermath of the incident at the startup in 2008, and to upgrade the experiments located on the LHC ring.

In 2015, the LHC restarted operations with Run 2, at an even higher center-of-mass energy of 13 TeV. During 2016 the design luminosity of 10^{34} cm^{-2}s^{-1} was exceeded and a total of 41 fb^{-1} of data were delivered. A comparison of the delivered integrated luminosity per year is shown in Figure 3.2.
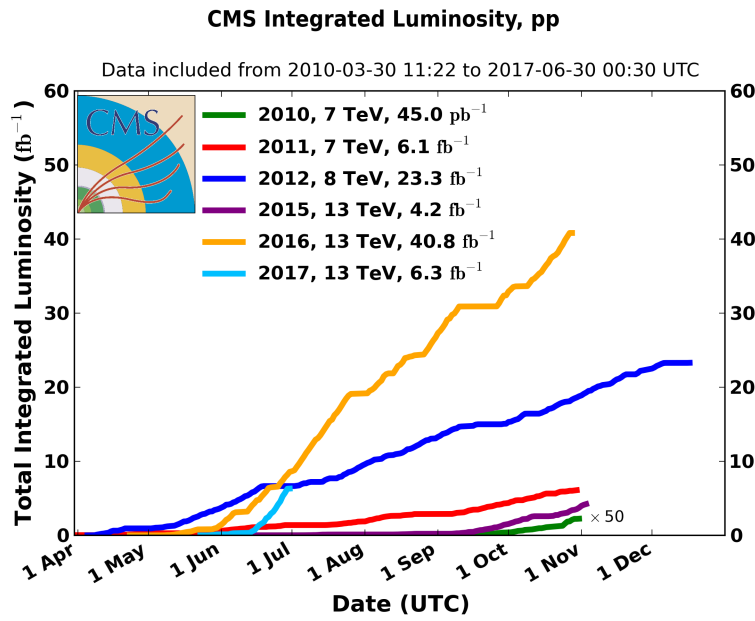

Figure 3.2: Overview of the integrated luminosity delivered to the CMS detector during Run 1 (2010 to 2012) and Run 2 (2015 to 2017).

3.1.3 The experiments at the LHC

There are four interaction points (IPs) where the proton or lead ion beams of the LHC can collide, and around each of these points large particle detectors were built in order to record the generated collisions. The ATLAS and CMS detectors, located at IP1 and IP5, are both high luminosity general-purpose detectors and are consist of several layers surrounding the IP in an onion-like structure to avoid particles escaping detection. These detectors can cover a wide range of high energy physics, from precision measurements of the Standard Model to searches beyond the Standard Model. At IP2 the ALICE detector is specialized in heavy ion collisions with low instantaneous luminosities, around 10^{27} cm^{-2}s^{-1}. With this detector information is gathered about the quark-gluon plasma, a state of matter that exists at extremely high temperatures and/or densities where quarks and gluons are no longer confined in hadrons. The fourth main detector, LHCb is located at IP8 and requires medium instantaneous luminosities of the order of a few 10^{32} cm^{-2}s^{-1}. Using this detector b quarks are being studied, focusing on the matter-antimatter asymmetry.

3.2   The CMS detector

The searches described in this thesis were conducted using data collected at the CMS detector, a general-purpose particle physics detector located on the LHC ring. The detector consists of the typical components of a particle physics detector, namely a tracker, an electromagnetic calorimeter (ECAL), a hadronic calorimeter (HCAL), a solenoidal magnet, and muon detectors. One peculiar aspect is however that both calorimeters are situated inside the superconducting magnet. This design was chosen in order to improve the energy resolution by reducing the amount of material in front of the calorimeters. The detector has a length of 21.6 m, a diameter of 14.6 m and a total weight of 12500 t. A schematic overview of the CMS detector is shown in Figure 3.3.
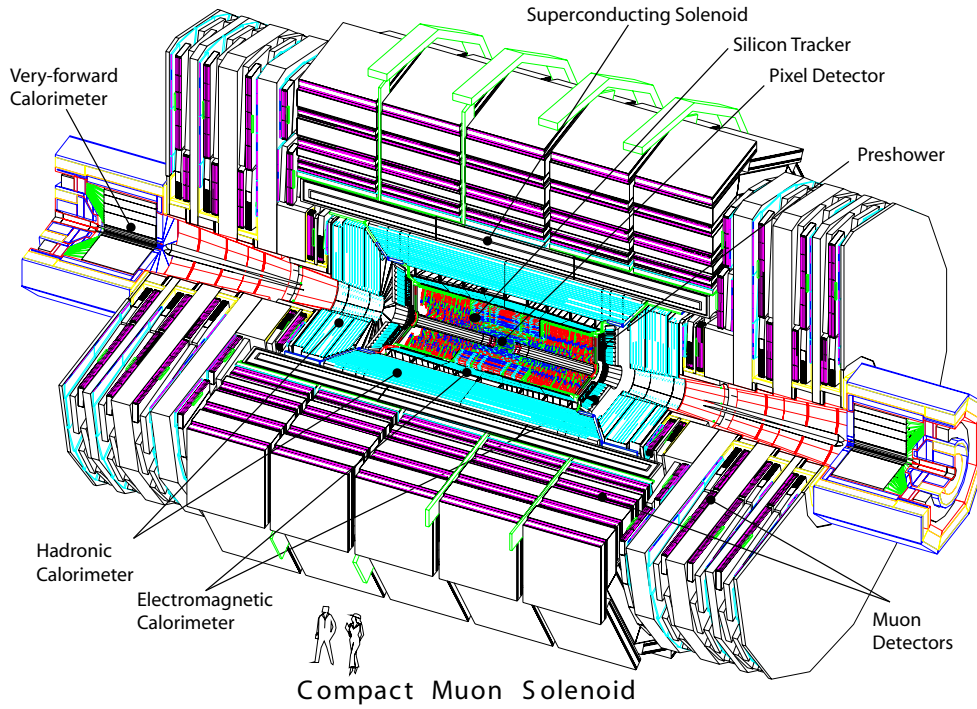

Figure 3.3: The CMS detector, consisting of the pixel and strip tracker, the electromagnetic calorimeter (ECAL) with preshower, the hadronic calorimeter (HCAL) with its forward component, and the muon systems.

The CMS coordinate system places the origin at the nominal collision point. The x axis is perpendicular to the beam and point towards the center of the LHC ring, the y axis is vertical and pointing upwards, and the z axis is defined anti-clockwise along the beam direction. The azimuthal angle ϕ is then defined in the xy plane, relative the the x axis and the polar angle θ is measured with respect to the z axis. In general, the polar angle is converted into the pseudorapidity

$$\eta = -\ln\left(\tan\frac{\theta}{2}\right) \tag{3.3}$$

for convenience, since differences in pseudorapidity are invariant under Lorentz boosts along the z axis. A pseudorapidity of 0 corresponds to the direction perpendicular to the beam ($\theta = \pi/2$), and an infinite pseudorapidity corresponds to the direction parallel to the beam ($\theta = 0$).

Due to the conservation of momentum before and after the collision, the momenta of the particles in the final state of a collision should be balanced in the transverse plane. Another variable that is therefore often used in particle physics is the transverse momentum of a particle, defined as

$$p_T = p \cdot \sin\theta. \tag{3.4}$$

3.2.1 The tracker

The innermost part of the CMS detector, closest to the IP, is the tracking system, which is designed to provide a precise measurement of the trajectory of charged particles. This all-silicon detector is divided into a pixel and a strip detector, with a layout as shown in Figure 3.4. The inner part, consisting of pixel modules, provides very precise 3D hits, which are important for vertex reconstruction and track seeding. This allows to have a precise measurement of secondary vertices and track impact parameters, necessary for the efficient identification of e.g. heavy flavor particles. As the hit occupancy is lower in the outer part of the detector, a larger cell size can be afforded, and silicon strips are used instead of pixels. This strip detector provides a large level arm and a link to the calorimeters and the muon system. The tracker covers a pseudorapidity range $-2.5 < \eta < 2.5$.
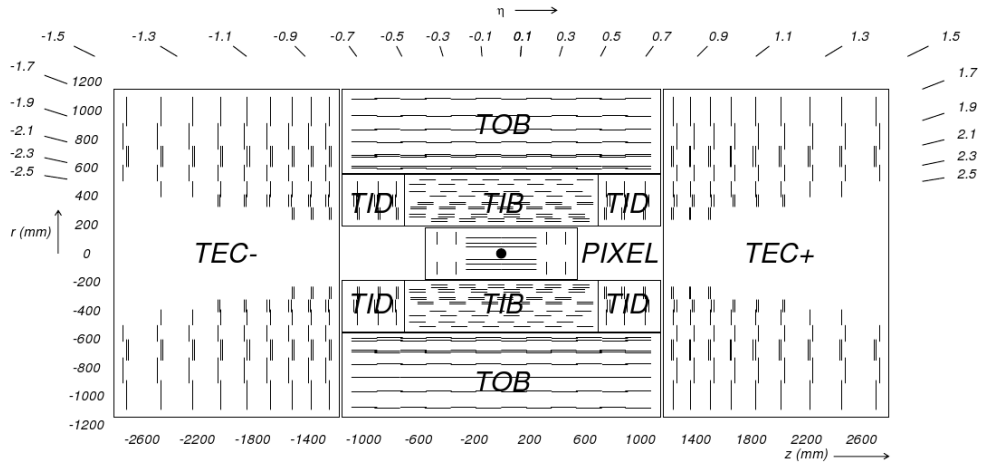

Figure 3.4: A transverse view of the pixel and strip tracker detectors.

3.2.1.1 The pixel tracker

The pixel tracker described here is the Phase 0 detector which was used to record the data used in this thesis, present for data-taking until 2016. During the extended technical stop in 2016 and 2017, it was replaced as a part of the CMS Phase 1 upgrades.

For the pixel modules n+ pixels on n-substrate are used, allowing the sensors to also work in under-depletion after type inversion. The 1440 modules are arranged in several cylindrical layers and disks, as illustrated in Figure 3.4. The barrel, consisting of 3 pixel layers surrounding the beam pipe at radii of 4.4, 7.3 and 10.2 cm, is complemented by the forward pixel detector, composed of 2 endcap disks on each side extending from 6 to 15 cm in radius. The barrel and the forward parts contain respectively 48 million and 18 million pixels with a size of $100 \times 150 \ \mu\mathrm{m}^2$, covering a total area of 1.06 m^2.

In the barrel, the magnetic field of CMS is perpendicular to the drift of the electrons to the collecting pixels, which results in a Lorentz drift. This drift leads to a spread of the charge over several pixels. Since the read-out of the modules is analog, an improved spatial resolution can therefore be achieved with charge interpolation. In the forward pixel detector the drift of the electrons would be parallel to the magnetic field so in order to profit from the Lorentz angle, the modules are tilted by 20° in a turbine-like arrangement, as can be seen in Figure 3.5. A spatial resolution of 10 μm (30 μm) can be achieved in the local directions x (y) of the module, respectively. In the barrel x is the longitudinal direction perpendicular the the beam and y is the longitudinal direction parallel to the beam.

The signals from the pixel sensors are read out by custom read-out chips (ROCs), which amplify and store the signals, and already apply zero-suppression on-detector. The data rate from the detector to the Front End Drivers (FEDs) is therefore not constant for every event. Additionally, if there are too many hits on a pixel module for a given event, they can not all be stored on the finite buffer of the ROC. Consequently, as the instantaneous luminosity increases the pixel modules start to show a "dynamic
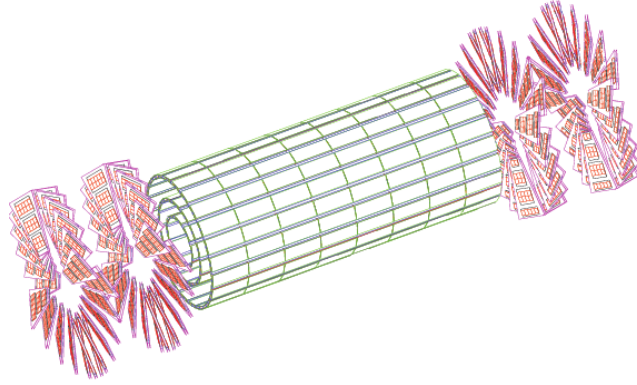
Figure 3.5: A 3D view of the barrel and forward pixel detector.

inefficiency" which is most pronounced in the first layer, closest to the beampipe. This was one of the main motivations for the Phase 1 upgrade of the pixel detector.

3.2.1.2   The strip tracker

The outer part of the tracker consists of 15 148 strip modules, which are distributed among multiple barrel layers and endcap disks and make up a total active area of 198 m^2. The inner part is composed of 4 Tracker Inner Barrel (TIB) layers with 3 Tracker Inner Disks (TID) on each side. Surrounding these are 6 Tracker Outer Barrel (TOB) layers and the 2 Tracker EndCaps (TEC), which are composed of 9 disks. This geometric arrangement is shown in Figure 3.4, with double lines to indicate back-to-back modules. These so-called double-sided modules are mounted with a stereo angle of 100 mrad to improve the 3D point resolution by providing a measurement of the z and r co-ordinate in the barrel and disks, respectively.

In the TOB and the 3 outermost rings of the TEC two silicon sensors are daisy chained, while single sensors are used in the inner part. This is done to limit the number of read-out channels, since the area that had to be instrumented is larger in the outer region. The larger cell size can be afforded due to the lower occupancy in the outer part. However, the noise of the sensors also increases with strip length, so thicker silicon sensors, 500 μm compared to 320μm in the inner part, are used in order to collect more signal per traversing particle.

The strip sensors are single sided p-on-n type silicon. The signals from the sensors are amplified, shaped, and stored by 4 or 6 custom APV25 chips per module. When the trigger has made a positive decision, the analog signals from two APV25 chips are multiplexed and sent to the FED boards in the service cavern via optical fibers, where they are converted to digital signals. The FEDs then perform pedestal and common mode subtraction as well as cluster finding. Additionally, the data is sparsified in these off-detector electronics, before being sent to the CMS central data acquisition (DAQ). Due to charge sharing, this analog read-out scheme also results in an improved spatial resolution of 15 to 40 μm, depending on the position of the modules and the strip pitch.

3.2.1.3   Tracking

The tracks of charged particles going through the CMS tracker are reconstructed with an iterative tracking algorithm. This approach is used to cope with the high occupancy and consequently high combinatorics. Additionally, the first iterations search for tracks with less possible combinations, such as tracks with many pixel hits or a high momentum. After every iteration, the hits associated with the found track are removed to reduce the combinatorics. Each iteration consists of four steps:

1. **Seed generation.** In this first step hits are combined into seeds for the subsequent track finding. In the initial iterations pixel triplets are used, then pixel pairs, in order to take gaps or non-working modules into account. Next, mixed pixel/strip triplets are taken, and finally strip-only hits are used.

These additional iterations improve the acceptance in p_T or in displacement with respect to the primary vertex.

2. **Track finding**. The seeds are used as starting point for a Kalman filter algorithm. This method extrapolates the seed trajectory outward to the next layer, taking into account potential energy loss and multiple scattering. If compatible hits are found in the next layer, the parameters of the trajectory are updated. This process continues until the outermost layer of the tracking system. Using this method, a given seed can generate multiple tracks, or different tracks can share hits. A trajectory cleaner therefore determines the fraction of hits the tracks have in common and discards the track with the lowest number of hits when there are too many shared hits. If both tracks have the same number of hits, the track with the largest χ^2 value is removed.

3. **Track fitting.** The track parameters are then refitted using a Kalman filter and smoother, taking all hits determined in the track finding step into account.

4. **Track selection.** Finally, the tracks are selected based on quality requirements, such as the number of layers that have hits, the χ^2/dof, and the distance to a primary vertex. This greatly reduces the fraction of reconstructed tracks that are fake.

The performance of the track reconstruction is excellent, and a high track-finding efficiency is obtained while keeping the rate of fake tracks negligible. The highest tracking efficiency is obtained for muons, which traverse the full volume and have an improved momentum resolution due to tracking information from the muon detectors giving a long lever arm. For isolated muons with p_T between 1 and 100 GeV the tracking efficiency is higher than 99% for the entire η coverage of the tracker. The p_T resolution is about 2-3% for a muon with $p_T = 100$ GeV up to $|\eta| < 1.6$, but increases for higher pseudorapidities. Different types of particles will interact differently with the detector material. Charged hadrons, for example, are also subject to elastic and inelastic nuclear interactions and have a tracking efficiency of 80-95% depending on pseudorapidity and transverse momentum.

Finally, the primary vertex is reconstructed from the tracks. This is done in 2 steps: first the tracks that appear to originate from the same interaction vertex are clustered, then a fitting procedure computes the vertex parameters and assigns a weight to each associated track, reflecting the probability that it corresponds to the considered vertex. Figure 3.6 shows the reconstruction efficiency and the resolution of the primary vertex. The more tracks, the better the vertex is constrained and thus the better the resolution.
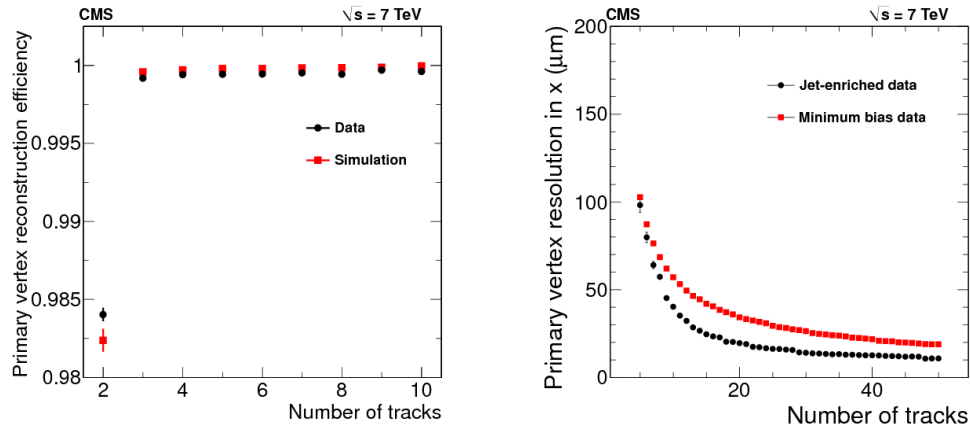

Figure 3.6: The primary vertex reconstruction efficiency (left) and resolution (right) as a function of the number of tracks associated to it.

3.2.2 The electromagnetic calorimeter

Surrounding the tracker, the CMS electromagnetic calorimeter (ECAL) is designed to measure the energy of photons and electrons. It is composed of 75 848 lead tungstate ($PbWO_4$) crystals arranged in a cylindrical barrel and 2 endcaps. This high density material was chosen due to its short radiation length and

small Moliére radius, resulting in a small spread of the electromagnetic shower generated by an incoming photon or electron. This leads to a fine granularity, a better shower separation, and a compact calorimeter. Additionally, this scintillating material has a fast response, as about 80% of the light is emitted during the first 25 ns. The scintillation light is collected by photodetectors, digitized, and read out.

The layout of the ECAL is shown in Figure 3.7, with the barrel (EB) extending up to $|\eta| < 1.470$ and the endcaps (EE) on each side covering the range $1.479 < |\eta| < 3.0$. A preshower detector (ES) is positioned in front of the endcap crystals, covering the pseudorapidity range between $|\eta| = 1.653$ and $|\eta| = 2.6$. This detector consists of a layer of lead which initiates an electromagnetic shower from incoming photons or electrons, and a layer of silicon sensors which measures the deposited energy. The main goal of this 20 cm thick detector is to discriminate between photons and neutral pions.
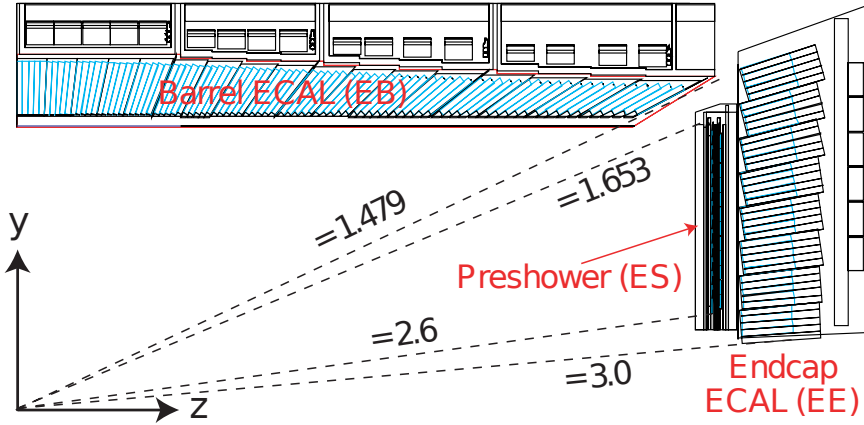

Figure 3.7: A transverse view parallel to the beamline showing one quarter of the ECAL, with its barrel (EB), endcap (EE), and preshower (ES) detectors.

The energy resolution of calorimeters can be parametrized by the following stochastic (S), noise (N), and constant (C) terms:

$$\left(\frac{\sigma}{E}\right)^2 = \left(\frac{S}{\sqrt{E}}\right)^2 + \left(\frac{N}{E}\right)^2 + C^2 \tag{3.5}$$

The stochastic term represents contributions from the shower containment, the number of photoelectrons and the fluctuations in the gain process. The noise term takes into account all noise components, such as electronics and digitization noise. Finally, the constant term characterizes among others energy leakage from the back of the calorimeter crystals and non-uniformities of the longitudinal light collection. The latter term dominates the energy resolution for high-energy electron and photon showers. Figure 3.8 shows the energy dependence of this resolution for incident electrons as measured in a beam test, as well as the determined stochastic, noise, and constant terms obtained by fitting equation 3.5 to the data.

A more recent measurement of the energy resolution was performed using electrons from Z boson decays in collision data. In the central region, up to $|\eta| < 0.8$, it was measured to be better than 2%. Outside of this region, in the more forward direction, the energy resolution is 2-5%. [1]

3.2.3 The hadronic calorimeter

The hadronic calorimeter (HCAL) surrounds the ECAL with the aim to measure the energy of hadrons and neutrinos or exotic particles resulting in apparent missing transverse energy. This detector consists of brass absorber plates interleaved with plastic scintillator tiles.

Figure 3.9 shows a longitudinal quarter view of the different HCAL components. A cylindrical barrel (HB) covers the region up to $|\eta| < 1.4$ and is complemented by endcaps (HE) on each side, extending the pseudorapidity range to $|\eta| < 3.0$. In the central region, the stopping power of the ECAL and HCAL
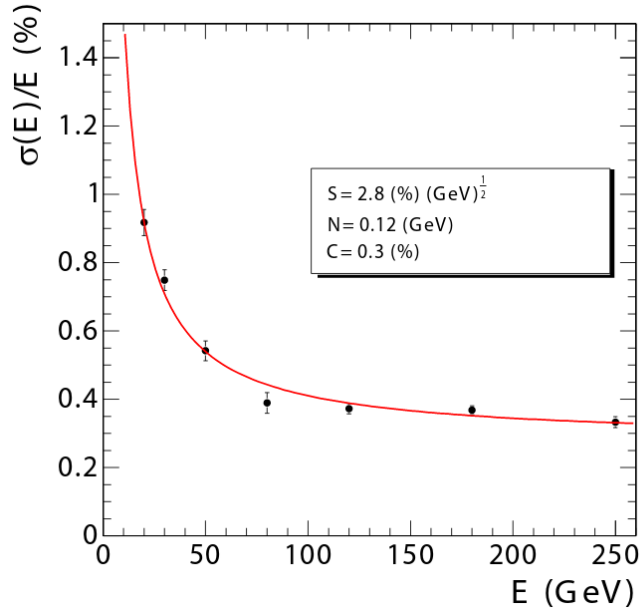
$$S = 2.8 \, (\%) \, (GeV)^{\frac{1}{2}}$$
$$N = 0.12 \, (GeV)$$
$$C = 0.3 \, (\%)$$

Figure 3.8: The ECAL energy resolution as a function of the electron energy, measured from a beam test. The stochastic (S), noise (N), and constant (C) are given as well.

1 barrel is not sufficient to contain the entire hadron showers. The HCAL was therefore extended outside
2 the solenoid with an outer calorimeter (HO), which uses the the magnet coil as absorber and consists of
3 scintillators. Two layers are positioned at $\eta = 0$, where the absorber depth is minimal, and only 1 layer is
4 used for the 2 rings on each side of the central ring. Finally, a forward calorimeter (HF) is positioned at
5 11.2 m from the IP covering $3.0 < |\eta| < 5.2$. Unlike the other HCAL components, this detector consists
6 of iron and quartz fibers. Cherenkov-based, radiation-hard technology, since it is exposed to very large
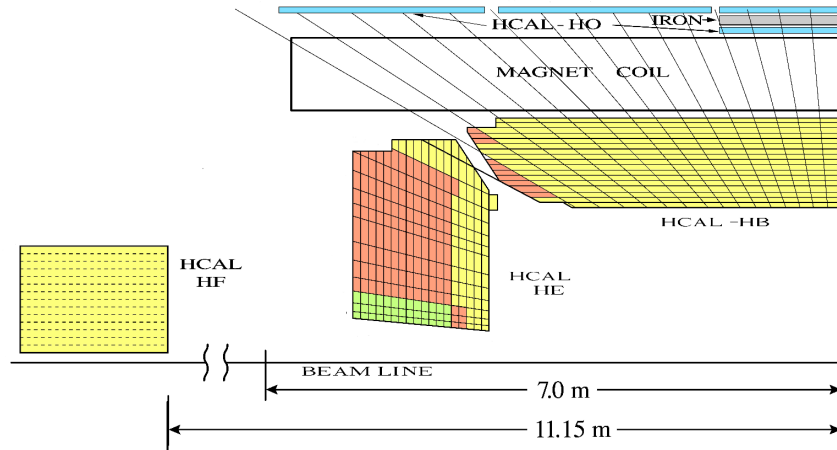7 particle fluxes.

Figure 3.9: A quarter view of the hadronic calorimeter (HCAL), parallel to the beamline. The barrel (HB), endcap (HE), outer (HO), and forward (HF) detectors are indicated.

8 The optical signals from the scintillators in HB, HE and HO are converted to electrical signals by
9 multichannel hybrid photodiodes. In the HF, the Cherenkov light emitted in the quartz fibers is detected
10 by standard photomultiplier tubes (PMTs), since the magnetic field is much smaller in this region.
11 The expected transverse energy resolution of jets is shown in Figure 3.10 for various pseudorapidity
12 regions: barrel jets ($|\eta| < 1.4$), endcap jets ($1.4 < |\eta| < 3.0$), and very forward jets ($3.0 < |\eta| < 5.0$).
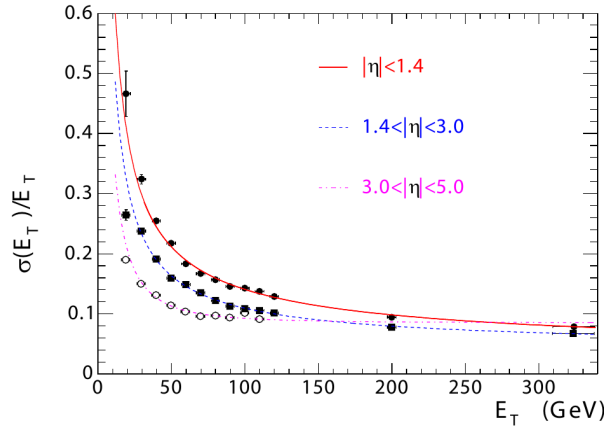
Figure 3.10: The jet transverse energy resolution as a function of the jet transverse energy, for barrel jets ($|\eta| < 1.4$), endcap jets ($1.4 < |\eta| < 3.0$), and very forward jets ($3.0 < |\eta| < 5.0$).

3.2.4 The muon system

The outermost detector, located entirely on the outside of the solenoid, is a dedicated muon system. The purpose of this subsystem is muon identification, momentum measurement, and triggering. As illustrated in Figure 3.11, the layers of muon chambers are embedded in the iron yoke closing the magnetic field lines.

Three different types of gaseous detectors are used. In the barrel, 4 layers of Drift Tubes (DT) are installed, covering the pseudorapidity range up to $|\eta| < 1.2$. Due the higher flux and the larger and non-uniform magnetic field at larger pseudorapidities, Cathode Strip Chambers (CSC) are used in the endcap region ($0.9 < |\eta| < 2.4$). The DTs are designed for the low muon rates that are expected in the barrel and thus have a slower response time than the CSCs. Resistive Plate Chamberss (RPCs) complement the DT and CSC systems in the pseudorapidity region up to $|\eta| < 1.6$. They provide a fast response, with a good time resolution but a worse spatial resolution than the DTs or CSCs. The RPCs therefore very well suited to trigger on muons.
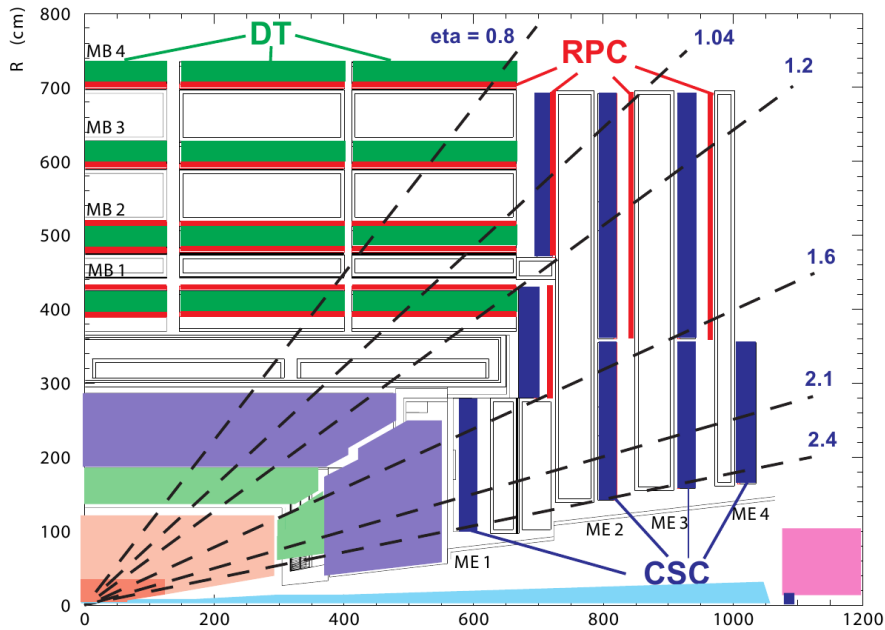

Figure 3.11: A transverse view of one quarter of CMS showing the position of the 3 types of muon detectors. The Drift Tubes (DT) are located in the barrel, the Cathode Strip Chambers (CSC) in the endcaps, and the Resistive Plate Chambers (RPC) in both regions up to $|\eta| < 1.6$.

The offline reconstruction efficiency of simulated single-muon samples is typically between 95% and 99%, except for the regions between 2 DT wheels ($|\eta| = 0.25$ and $|\eta| = 0.8$) and the transition region between the DTs and CSCs ($|\eta| = 1.2$), where the efficiency drops. For low pseudorapidities and small momenta, the offline momentum resolution of the standalone muon system is about 9%. At momenta around 1 TeV, the resolution varies from 15% to 40%, depending on the pseudorapidity. As demonstrated in Figure 3.12, performing a global momentum fit using the tracker as well improves the resolution by an order of magnitude at low muon momenta. At high momenta the resolution of the full system is about 5%.
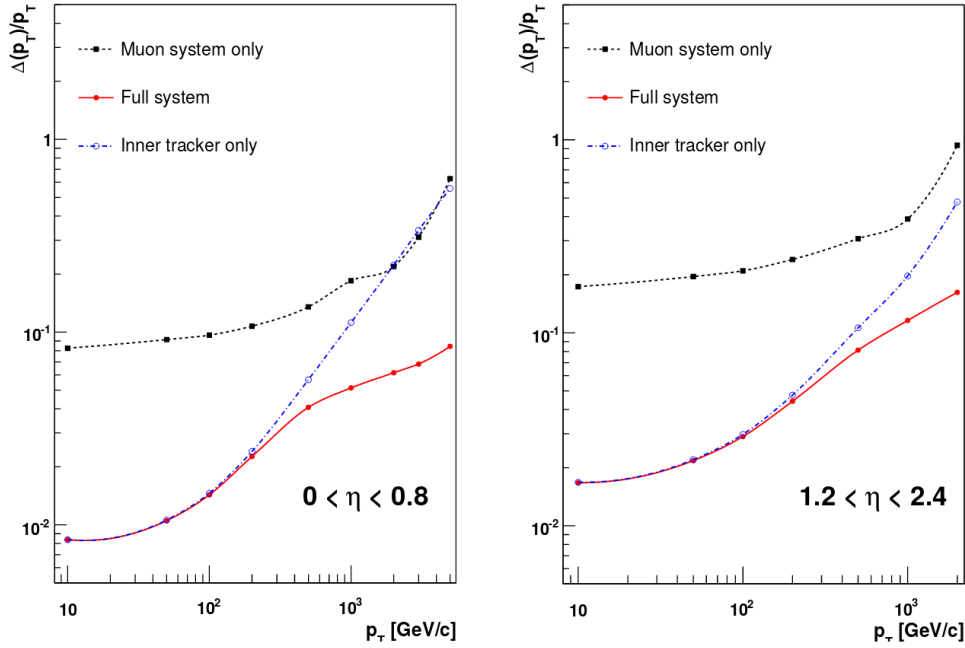

Figure 3.12: The muon transverse momentum resolution as a function of transverse momentum for low (left) and (high) pseudorapidities. The resolution is shown for the muon system and the tracker separately, and for the full system.

3.2.5 Trigger and data acquisition

Collisions are provided by the LHC at high interaction rates, with an interval of 25 ns between bunch crossings. This corresponds to a frequency of 40 MHz. Additionally, multiple collisions occur at the same time, depending on the luminosity. Since it is impossible to store and process the large amount of data produced in the collisions at this high rate, a severe rate reduction is needed. This rate reduction is performed by the trigger system, which decides whether to store or reject an event. Since this decision must be made every 25 ns, the complexity of the trigger system is limited and the computing time is optimized by rejecting uninteresting events as quickly as possible. The rate is reduced to 100 Hz in 2 steps by the Level-1 (L1) Trigger and the High-Level Trigger (HLT).

The L1 Trigger decision is based on information from the calorimeters and muon systems. At the lowest level, the Local Triggers are based on energy deposits in calorimeter towers and track segments or hit patterns in the muon system. Regional Triggers then combine this information and use pattern logic to determine trigger objects such as electron or muon candidates in separated spatial regions. The candidates are ranked based on their energy or momentum and quality. Finally, the Global Calorimeter and Global Muon Triggers determine the highest-rank calorimeter and muon objects across the whole detector and transfer them to the Global Trigger, which makes the final decision to accept or reject an event. Following this procedure, the L1 Trigger reduces the event rate to 100 kHz. The L1 Trigger is composed of custom electronics located partially on the detectors, and partially in the underground service cavern. The L1 decision needs to be made and distributed to the detector front-end electronics within 3.2 μs.

In the second step, the HLT reduces the event rate further to 100 Hz. The complete read-out data, including the tracker information, is available for this step. More complex calculations can therefore be performed, speed-optimized but similar to those made in the offline software. In contrast to the L1 Trigger, the HLT software system is implemented in a filter farm of about 1000 commercial processors.

3.2.6   CMS performance in Run 2

The number of collisions recorded at the experiments can differ from the amount delivered by the LHC. This downtime can e.g. be caused by problems with a particular subdetector, the trigger rate, the data acquisition, or the infrastructure. During Run 2, CMS achieved a data taking efficiency of 89% and 92% in 2015 and 2016, respectively. The comparison between the delivered and recorded cumulative integrated luminosity in 2016 is shown in Figure 3.13. Subsequently, the recorded data is certified by the offline Data Quality Monitoring (DQM), to ensure that the data is suited for physics analysis.
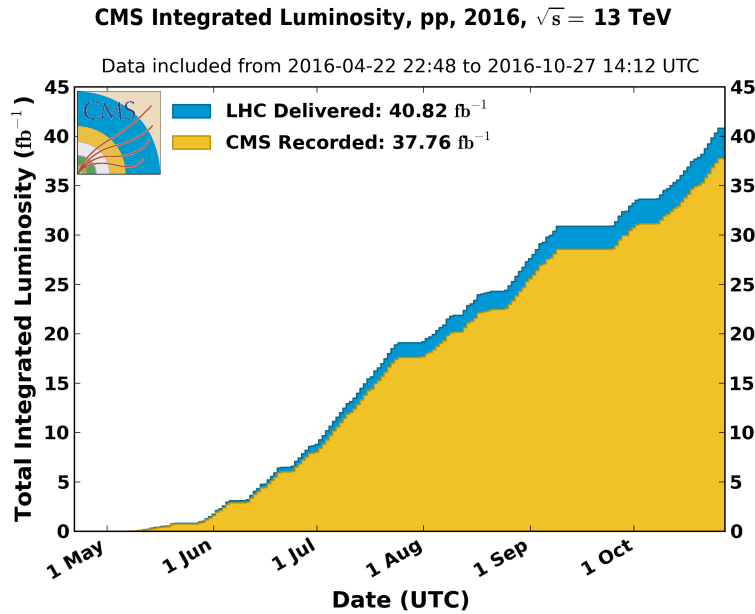
CMS Integrated Luminosity, pp, 2016, $\sqrt{s} = 13$ TeV

Data included from 2016-04-22 22:48 to 2016-10-27 14:12 UTC

LHC Delivered: 40.82 fb^{-1}
CMS Recorded: 37.76 fb^{-1}

Figure 3.13: The cumulative distribution of the instantaneous luminosity delivered by the LHC (blue) and recorded by CMS (yellow) in 2016.

3.2.6.1   Pre-amplifier saturation in the APV25 chip

During Run 2, the instantaneous luminosity delivered by the LHC increased continuously, and even exceeded the design luminosity of 10^{34} cm^{-2}s^{-1} in 2016. As the luminosity increased, a dynamic inefficiency appeared in the strip tracker, which was most noticeable in the first layer of the TOB. The symptoms were a change in the signal-to-noise ratio and loss of hits. As can be seen from Figure 3.14, the most probable value (MPV) of the signal-to-noise ratio is shifted towards lower values and the low tail increased as well. The loss of hits is clearly visible in left plot of Figure 3.15, showing the number of hits per track per run period. The number of hits decreases for run periods B to F, as the instantaneous luminosity increased, and is shifted to higher values again in run periods G and H, when the dynamic inefficiency was cured. The loss of hits results in less and shorter tracks, which is also reflected in the fraction of charged energy in jets, shown in the right plot of Figure 3.15.

The origin of this inefficiency was eventually tracked down to saturation effects in the pre-amplifier of the APV25 chip. The pre-amplifier decay time changes significantly with temperature. As the temperature of the strip tracker was lowered from $+4°$C to $-15°$C during LS1, the decay time was no longer sufficient to cope with the high luminosities. The dynamic inefficiency was therefore cured in August
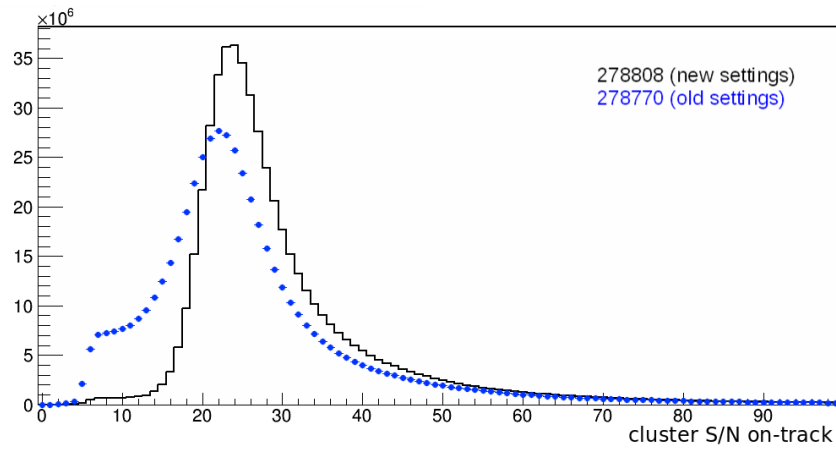
Figure 3.14: The signal-to-noise ratio in the first layer of the TOB for a run before (blue) and after (black) the change of pre-amplifier drain speed which cured the dynamic inefficiency.
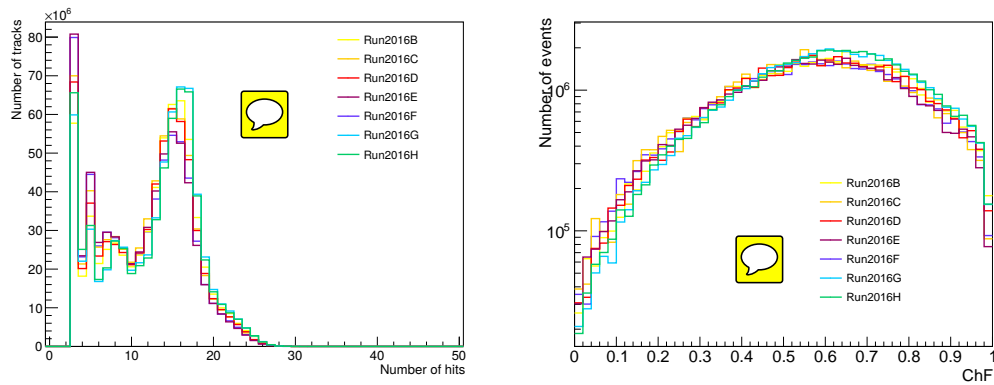

Figure 3.15: The number of hits per track (left) and the jet charged energy fraction (right) per run period in 2016. The instantaneous luminosity increased over the course of the year. The effect of the change of pre-amplifier drain speed, which cured the dynamic inefficiency, can be seen between run periods F and G.

2016 by changing the pre-amplifier drain speed. This lead among others to the recovery of the muon efficiency, which improved by 6 - 8% as demonstrated in Figure 3.16.
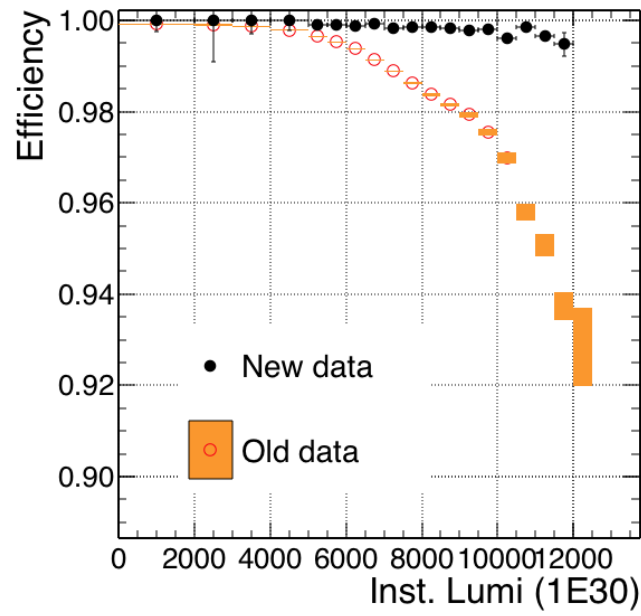
Figure 3.16: The muon efficiency as a function of the instantaneous luminosity for before (orange) and after (black) the change of pre-amplifier drain speed which cured the dynamic inefficiency.

4

Event Simulation and Reconstruction

4.1 Event generation

4.2 Detector simulation

4.2.1 Delphes

4.2.2 GEANT4

4.3 Event reconstruction

4.3.1 Electron reconstruction

4.3.2 Muon reconstruction

4.3.3 Jet reconstruction

4.3.4 B-tagging

4.3.5 Missing transverse energy reconstruction

4.3.6 Particle flow

4.4 Simulation of the SIMP signal

5

The Monojet Analysis

6

Search for SIMPs using Trackless Jets

7
Conclusion & Outlook

References

[1] Serguei Chatrchyan et al. *Energy Calibration and Resolution of the CMS Electromagnetic Calorimeter in pp Collisions at* $\sqrt{s} = 7$ *TeV*. JINST, 8:P09009, 2013. [JINST8,9009(2013)].

List of Acronyms

A

ATLAS   A Toroidal LHC ApparatuS

C

CERN   European Organization for Nuclear Research
CMS   Compact Muon Solenoid
CSC   Cathode Strip Chambers

D

DAQ   data acquisition
DQM   Data Quality Monitoring
DT   Drift Tubes

E

ECAL   electromagnetic calorimeter

F

FED   Front End Driver

H

HCAL   hadronic calorimeter
HLT   High-Level Trigger

I

IP   interaction point

L

L1   Level-1
LEIR   Low Energy Ion Ring
LEP   Large Electron Positron
LHC   Large Hadron Collider

P

PS   Proton Synchrotron
PSB   Proton Synchrotron Booster

R

RF   radio-frequency
ROC   read-out chip
RPC   Resistive Plate Chambers

S

SPS   Super Proton Synchrotron

T

TEC   Tracker EndCaps
TIB   Tracker Inner Barrel
TID   Tracker Inner Disks
TOB   Tracker Outer Barrel

1